Supporting Information

Redox-Active Sodium 3, 4-dihydroxy Anthraquinone-2-Sulfonate Anchored on Reduced Graphene Oxide for High-Performance Zn-ion Hybrid Capacitors

Kai Yang[a], Lei Hu[a], Yi Wang[a], Jianxing Xia[a], Mengxuan Sun[b],
Yunpeng Zhang[a], Chao Gou[a], Chunyang Jia[a, *]

[a]*State Key Laboratory of Electronic Thin Films and Integrated Devices, National Engineering Research Center of Electromagnetic Radiation Control Materials, School of Electronic Science and Engineering, University of Electronic Science and Technology of China, Chengdu 610054, P. R. China*

[b]*School of Physics, University of Electronic Science and Technology of China, Chengdu, 610054, P. R. China*

Experimental Section

Materials: Natural graphite powder was purchased from Shanghai Hua Yi Group Hua Yuan Chemical Industry Co, Ltd. (Shanghai). Sodium 3, 4-dihydroxy anthraquinone-2-sulfonate (ARS), $ZnSO_4$, and polyvinyl alcohol (PVA, hydrolyzed, medium molecular weight) were purchased from Sigma-Aldrich as reagent grades and used without further purifications. Deionized water (DIW) was used throughout this work.

Synthesis of PGAF-ARS and PGAF: Graphene oxide was synthesized by the traditional Hummers method, and the graphene oxide film was obtained by drying the GO (about 2 mg mL^{-1}) on a polyvinylidene fluoride (PVDF) plate. The PGAF-ARS composite was obtained by a simple one-step hydrothermal method. Particularly, the GOF was first immersed in ARS solution (the mass rate of ARS: GOF is x: y) and then transferred to Teflon-line high-pressure reactor for the hydrothermal reaction (4h at 180 °C). The autoclave was cooled to obtain porous graphene hydrogel films (PGHF-ARS), which were washed with deionized water three times, and the PGAF-ARS was obtained by freeze-drying eventually. In the control group, PGAF was treated the same as PGAF-

ARS except for the addition of ARS.

(ARS: GOF=x: y) Determination of the optimum proportion: In this experiment, we adjusted different ARS and GOF mass ratios to obtain the best electrochemical performance of graphene composites. As shown in **Fig. S1**, when we conducted the CV cycle test on PGAF-ARS prepared with different mass ratios, it was found that PGAF-ARS with a mass ratio of 1.5:1 had the higher capacitance. Meanwhile, for PGAF-ARS with a mass ratio of 1.5:1, the peak strength pair is much stronger than other ratios, showing a strong synergistic effect to a certain extent. The low ARS content in PGAF-ARS will lead to insufficient Faraday pseudo-capacitance (such as **Fig. S1b**). However, excessive ARS will hinder the porous path of graphene, which is not conducive to rapid ion transfer and even affect the overall electrochemical performance (such as **Fig. S1e**).[1, 2] Additionally, the additional of excessive ARS molecules with low conductivity will also reduce the conductivity of PGAF-ARS, it is detrimental to charge transmission. Besides, as described in BET in this work, the incorporation of too much ARS will lead to a decrease in specific surface area and electrochemical active sites, it is very detrimental to ion transport and electronic transfer. This conclusion has been verified in the GCD curve and specific capacitance curves at the same time (**Fig. S1g-i**), the 1.5:1 mass ratio shows the optimum capacity and capacitance performance. Therefore, we chose the 1.5:1 mass in this work.

DFT calculation: The DFT geometry optimizations were performed by CASTEP program codes, and the exchange-correlation interactions were described by generalized gradient approximation (GGA) with Perdew-Burke-Ernzerhof (PBE) function. For the slabs of graphene absorbed with the molecule and the graphene (001) clean surfaces were employed for integration in the reciprocal space. A vacuum layer of 20 Å was adopted to weaken the interactions between periodic images. The Monkhorst-Pack k-point mesh of 3×1×1 was used for the slabs and the convergence is 1×10^{-5} eV. The cutoff energy is set as 450 eV. The charge density difference was defined as follows:

$$\Delta \rho=\rho_{G\text{-}M}-\rho_{G}-\rho_{M} \qquad \text{S1}$$

where $\rho_{G\text{-}M}$, ρ_{G}, and ρ_{M} denote the charge density of the optimized graphene molecule interface, the corresponding separated graphene slab, and the molecule, respectively.

Galvanostatic intermittent titration technique (GITT): In this analysis, a current pulse of 0.5 A g^{-1} was applied for 50 s with a relaxation time of 1500 s. The GITT measurement is continued until the cut-off potential is reached at 25 °C shown in **Fig. 6e**. GITT calculation formula based on Fick's second law as follows:

$$D = \frac{4L^2}{\pi\tau}\left(\frac{\Delta E_s}{\Delta E_t}\right)^2 \qquad \text{S2}$$

where L is the thickness of the active materials (cm), approximately equal to the diffusion distance; τ corresponds to the galvanostatic pulse time (s); ΔE_s and ΔE_t represent the change value of quasi-equilibrium potential (V) resulting in the current pulse and the voltage change (V) during the current pulse, respectively.

Preparation of the gel electrode: The $ZnSO_4$/PVA gel was prepared by dissolving 1 g of PVA in 10 ml of $ZnSO_4$ aqueous solution (1 M) at 90°C.

Materials characterization: The crystal structure of the material was characterized by X-ray diffraction (XRD, Digaku D/mix 2400, CuKα 40 KV). The morphology and structure of the materials were characterized by a scanning electron microscope (SEM, GeminiSEM 300). The chemical states of elements on the surface of materials were measured by X-ray photoelectron spectroscopy (XPS, Thermo Scientific K-Alpha+). The defects and structures of the samples were analyzed by Semmer K-Dxrzxi Raman spectroscopy by using 633 nm laser excitation. Fourier transform infrared spectroscopy (FTIR) was recorded at Bruker Optik GmbH, INVENIO R's manufacturer. The contact angle of the material was measured by the JY-DHa contact angle tester. The N_2 adsorption and desorption isotherms of the materials were determined by an automatic specific surface and porosity analyzer. The sample was degassed at 120 °C for 6 h. BET and BJH calculations were used to characterize the specific surface and void distribution of materials (Mike ASAPZ 2460).

Electrochemical measurements: PGAF-ARS was cut into square pole pieces about ~1 cm × 1 cm in size and then attached to metal Pt foil. Subsequently, the ZIHCs were assembled with filter paper as the separator, 1 M $ZnSO_4$ as electrolyte and Zn sheet as the anode. Galvanostatic charge and discharge (GCD), and Cyclic Voltammetry (CV) curves for ZIHCs were measured on the CHI660E electrochemical working station. The CV and GCD curves ranged from 0.2-1.9 V. When not cycled, electrochemical impedance spectroscopy (EIS) of the ZIHCs was tested at 10^{-2}-10^{5} Hz frequency. For coin cell and FQS-ZIHCs, the galvanostatic charge and discharge stability tests were performed by using a battery test system (NEWARE, CT-ZWJ-4'S-T-1U). The specific capacitance (C_{ZIC}, mAh g^{-1}), energy density (E_{ZIC}, Wh kg^{-1}), and power density (P_{ZIC}, W kg^{-1}) of ZIHCs is calculated by equation S3, S4, and S5, respectively:

$$C_{ZIC} = \frac{I \times \Delta t}{3.6m} \tag{S3}$$

$$E_{ZIC} = \frac{\int VIdt}{A} \tag{S4}$$

$$P_{ZIC} = \frac{3600 \times E_{ZIC}}{\Delta t} \tag{S5}$$

where C_{ZIC} (mAh g^{-1}) is the specific capacity of ZIHCs (based on the weight of PGAF-ARS as the cathode material), I (A) is the discharge current, Δt (s) is the discharge time, m is the mass (g) of the film.

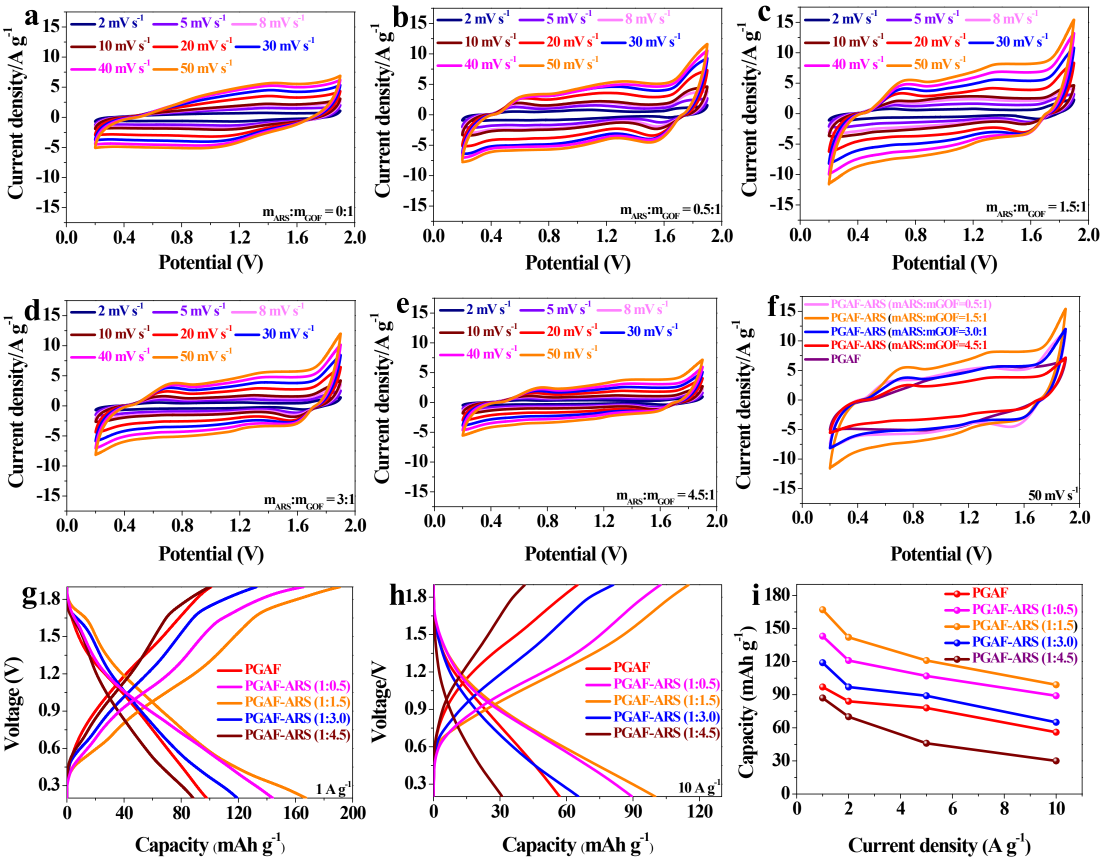

Fig. S1 (a-e) CV curves of PGAF and PGAF-ARS (different mass ratios) at different sweep speeds. (f) CV curves of PGAF and PGAF-ARS (different mass ratios) at 50 mV s^{-1}. (g-h) GCD curves of PGAF and PGAF-ARS (different mass ratios) at different current densities. (i) Specific capacitance of all samples at different current densities.

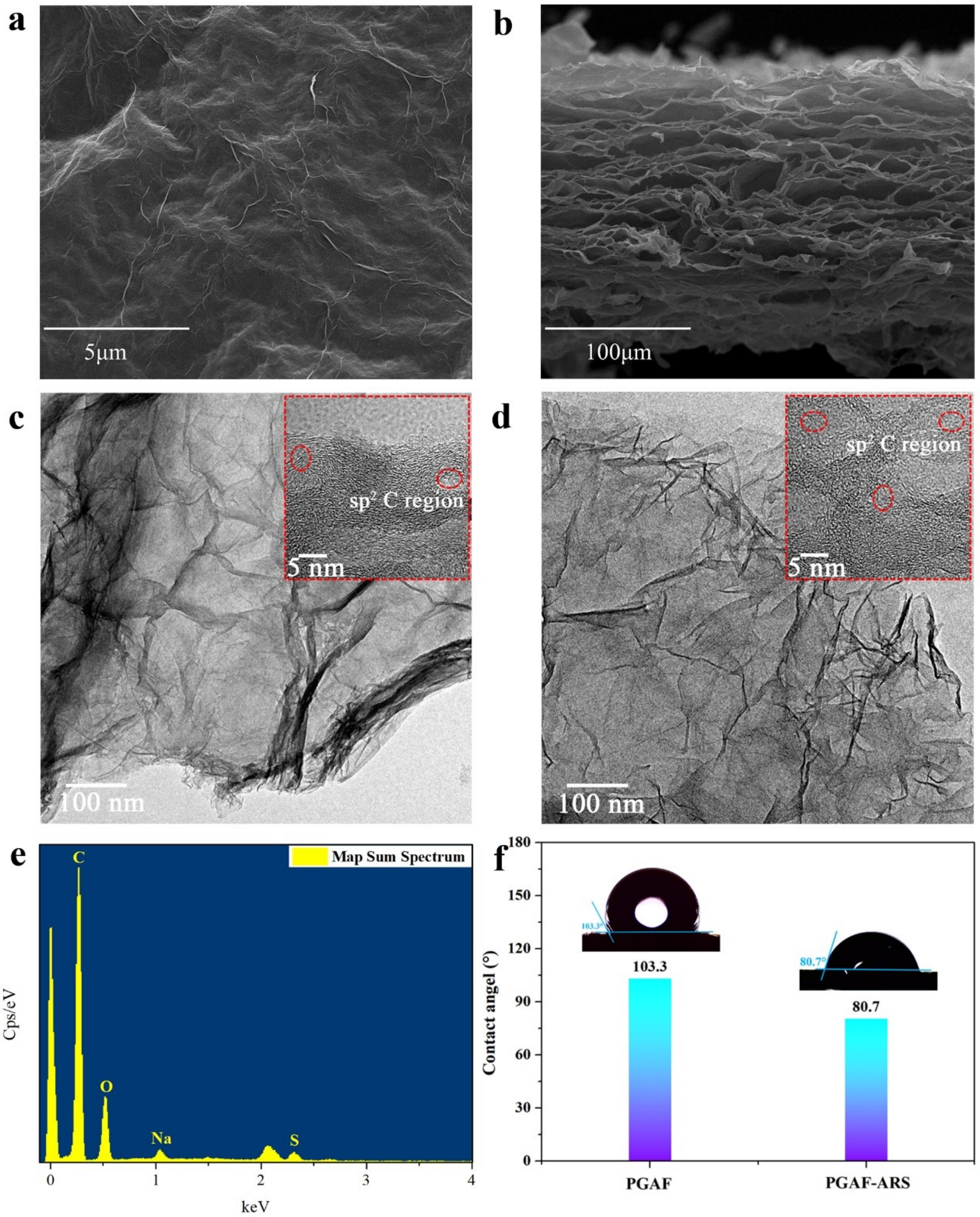

Fig. S2 Morphological characterization of PGAF composite. (a) SEM image and (b) Cross-section SEM image. (c) TEM image of PGAF-ARS. (d) TEM image of PGAF. (e) Mapping of PGAF-ARS. (f) The water contact angle of PGAF and PGAF-ARS.

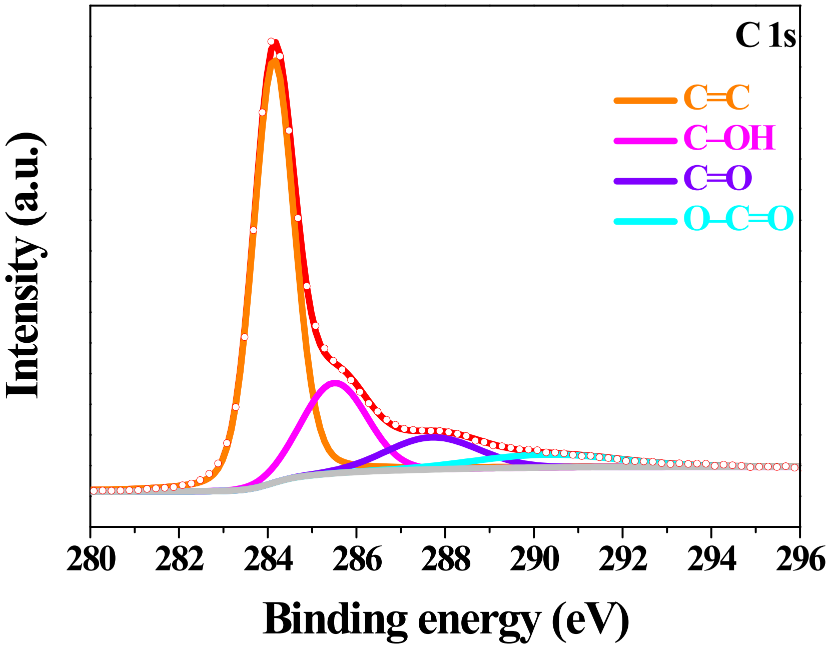

Fig. S3 The high-resolution XPS spectra of the C 1s region for PGAF.

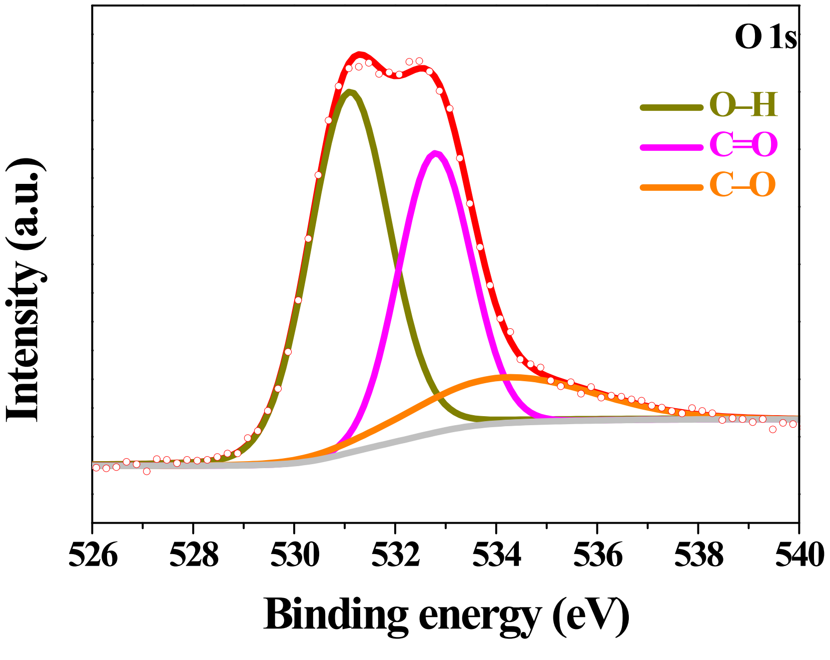

Fig. S4 The high-resolution XPS spectra of the O 1s region for PGAF-ARS.

As shown in **Fig. S4**, the O 1s spectrum of PGAF-ARS shows three different peaks corresponding to different functional groups: O-H (carboxylic groups) at 531 eV, C=O (quinone-type groups) at 533 eV, and C-O at 534.5 eV, respectively.

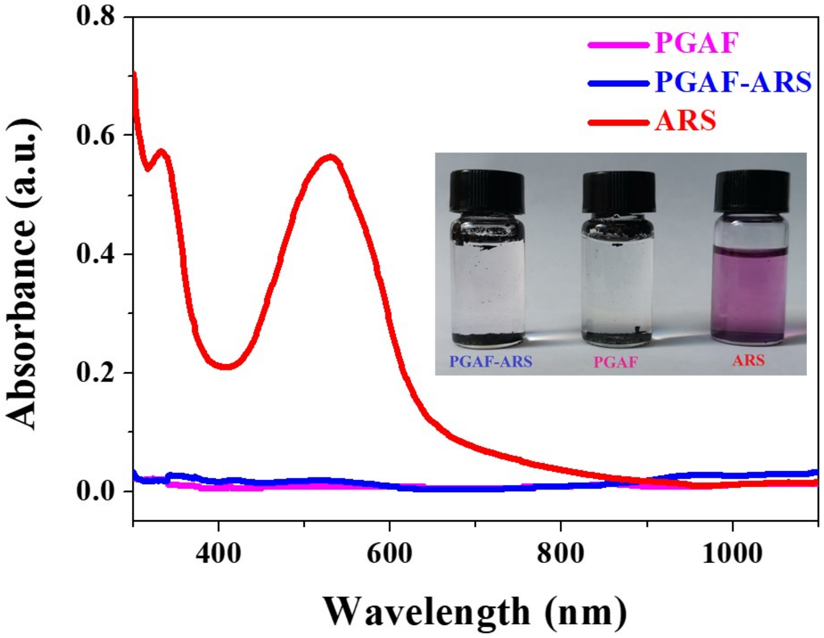

Fig. S5 UV-vis absorption spectra of ARS, PGAF, and PGAF-ARS solution, respectively. The image of the above solution is shown in the inset.

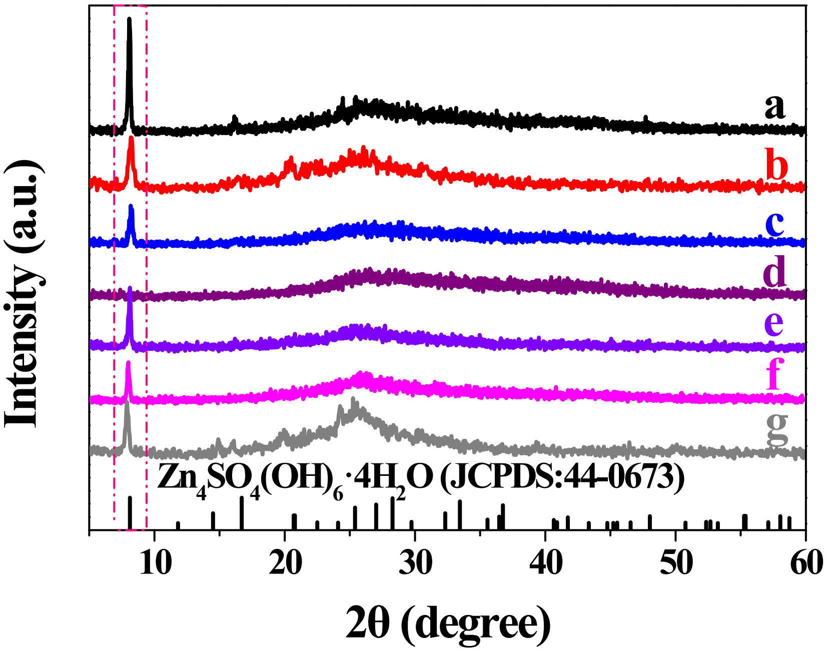

Fig S6 Ex-situ XRD spectra of the PGAF-ARS at different states. The red dashed boxes indicate the characteristic peaks of $Zn_4SO_4(OH)_6$•$4H_2O$. The dissolution and formation processes of $Zn_4SO_4(OH)_6$•$4H_2O$ are reversible at the charge and discharge process.

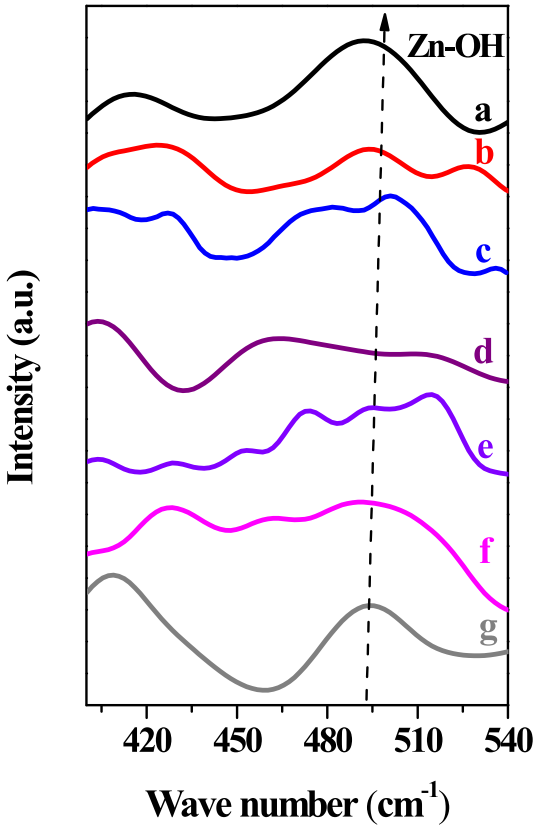

Fig. S7 Ex-situ Raman spectra of the PGAF-ARS at the different states.

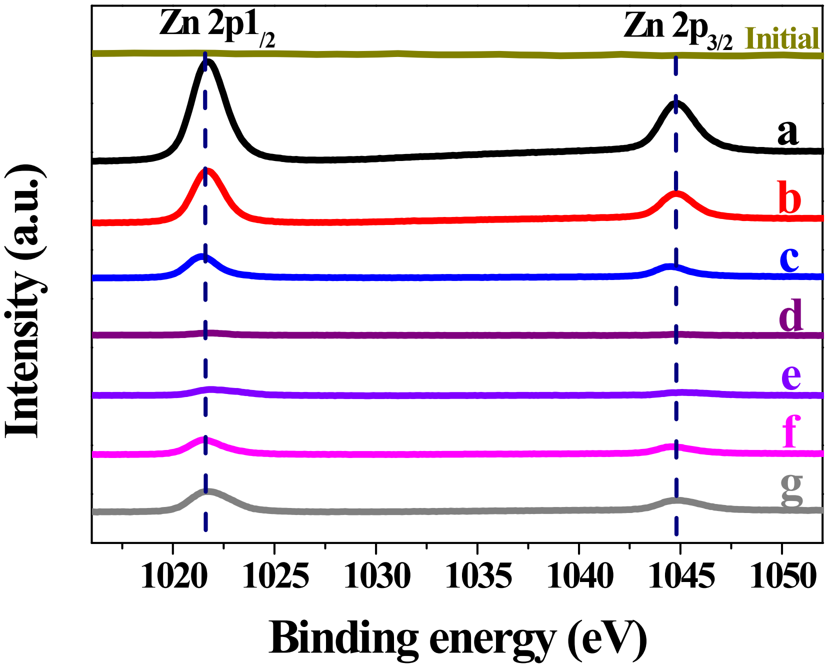

Fig S8 Ex-suit Zn 2p XPS spectra at the different selected states.

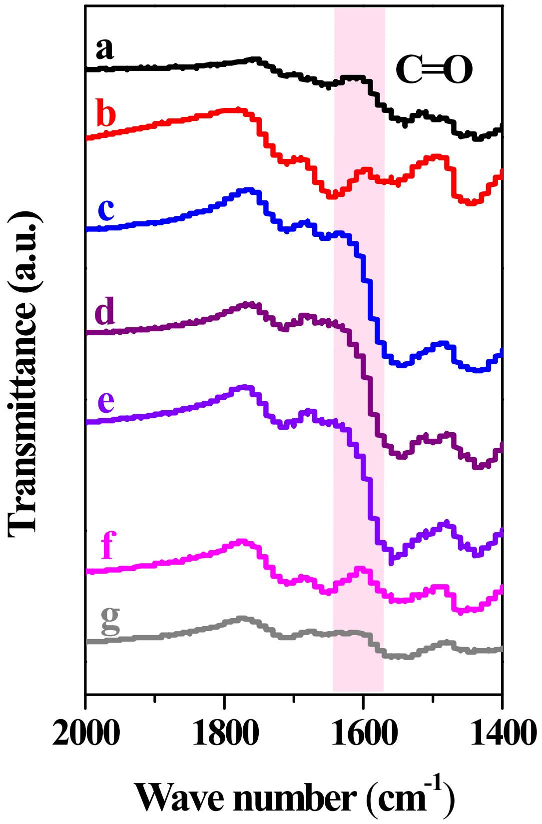

Fig. S9 Ex-situ FTIR spectra of the PGAF-ARS at the different states.

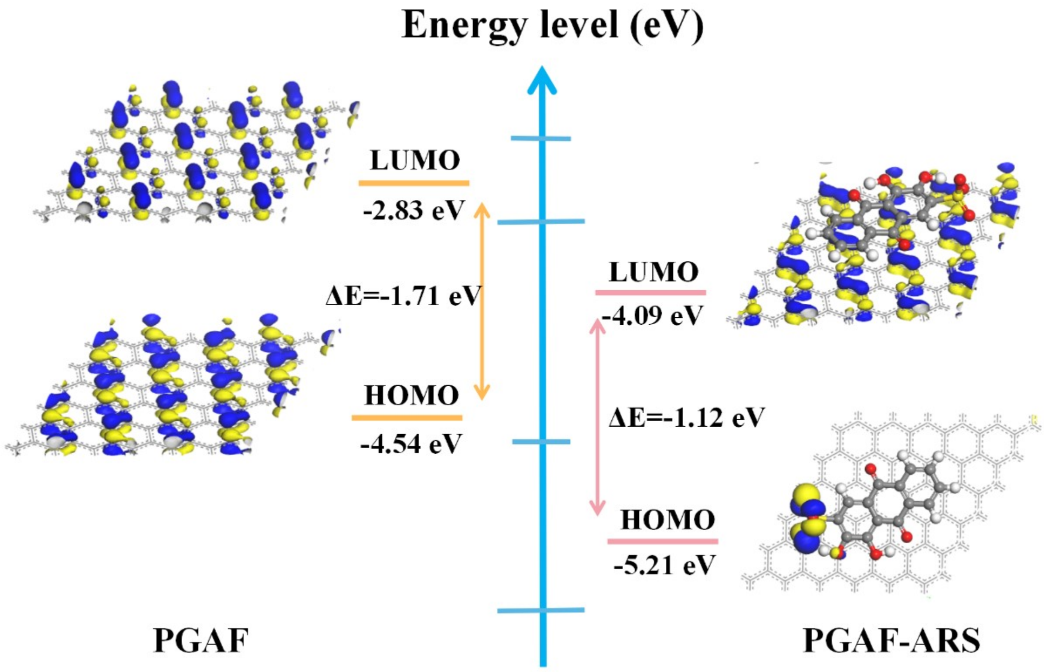

Fig. S10 Energy level diagram and frontier orbitals of PGAF and PGAF-ARS.

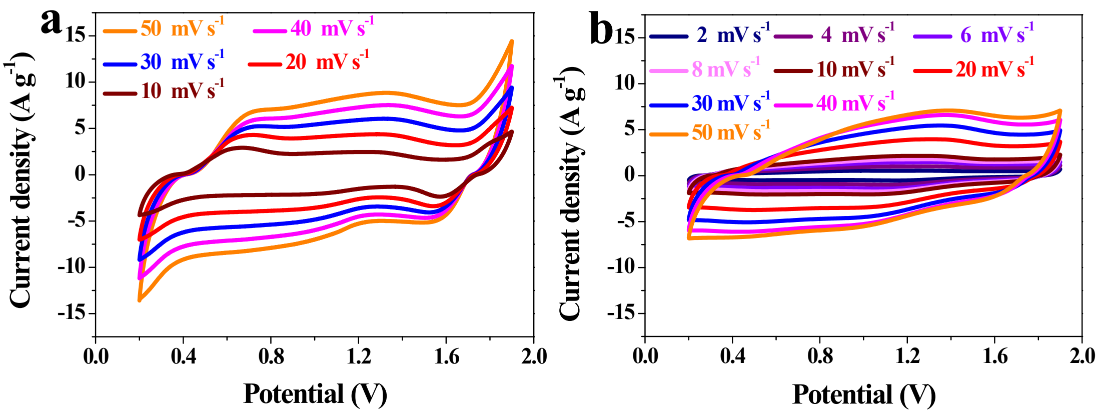

Fig. S11 (a) CV curves for PGAF-ARS at 10-50 mV s^{-1}. (b) CV curves for PGAF at a current density of 2-50 mV s^{-1}.

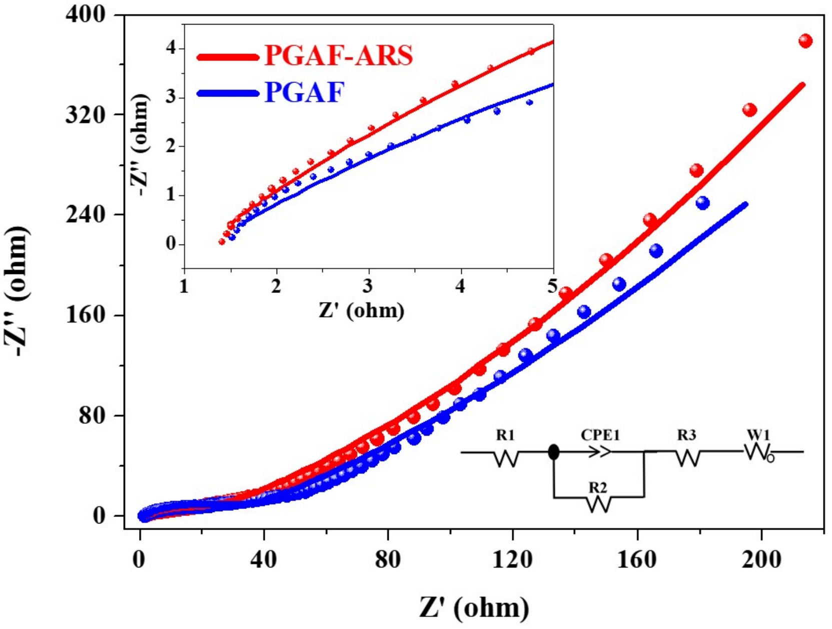

Fig. S12 Nyquist plots of PGAF-ARS and PGAF based on ZIHCs.

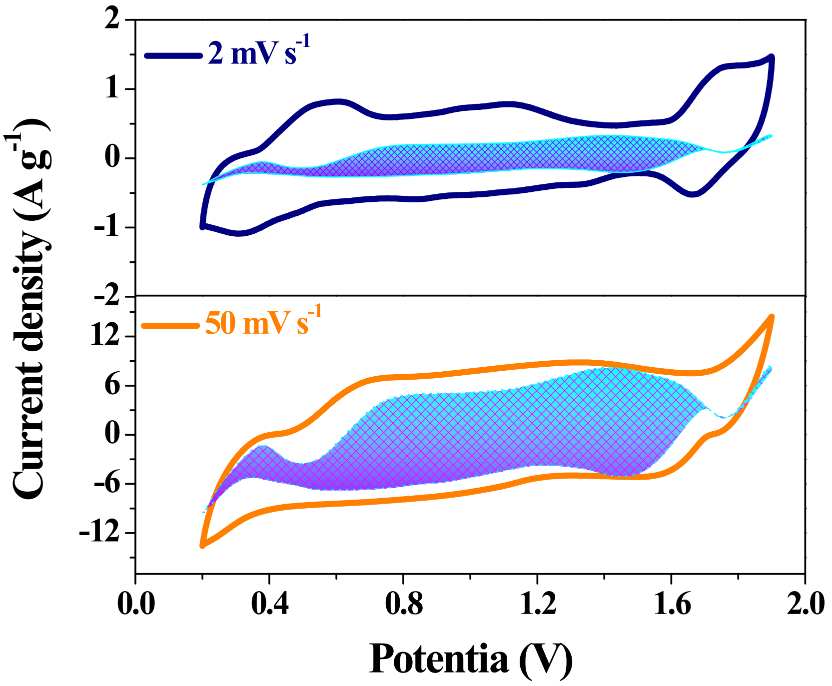

Fig. S13 CV curves at 2 mV s^{-1} and 50 mV s^{-1} with the shadowed area showing the surface-controlled capacitance of PGAF-ARS.

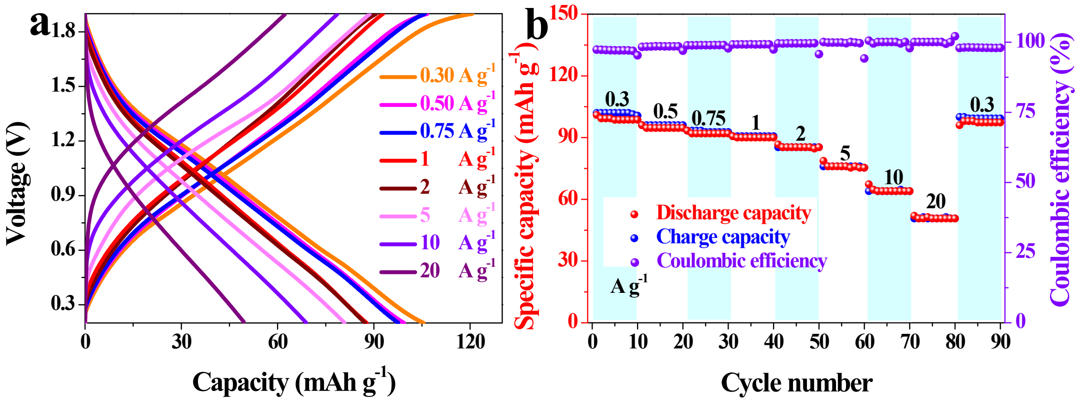

Fig. S14 (a) GCD profiles for PGAF at various current densities. (b) Rate capabilities from 0.3 to 20 A g^{-1} for PGAF.

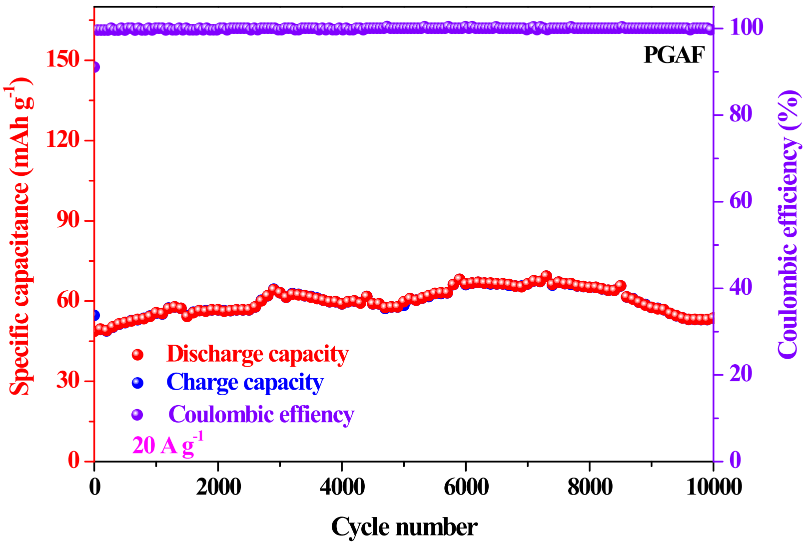

Fig. S15 Cycle stability and coulombic efficiency of PGAF based aqueous ZIHCs.

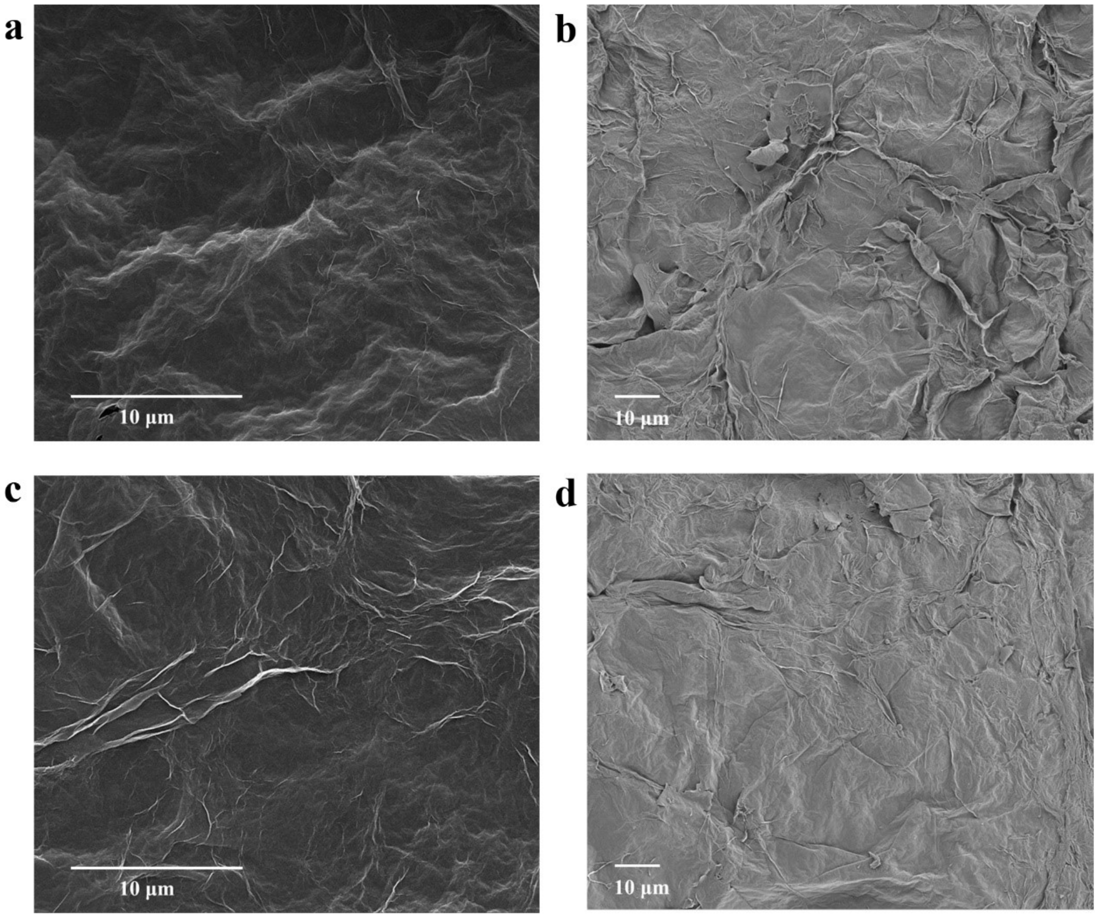

Fig. S16 (a) Initial SEM image of PGAF. (b) SEM image of PGAF after 10000 cycles at the current density of 20 A g^{-1}. (c) Initial SEM image of PGAF-ARS. (d) SEM image of PGAF-ARS after 10000 cycles at the current density of 20 A g^{-1}.

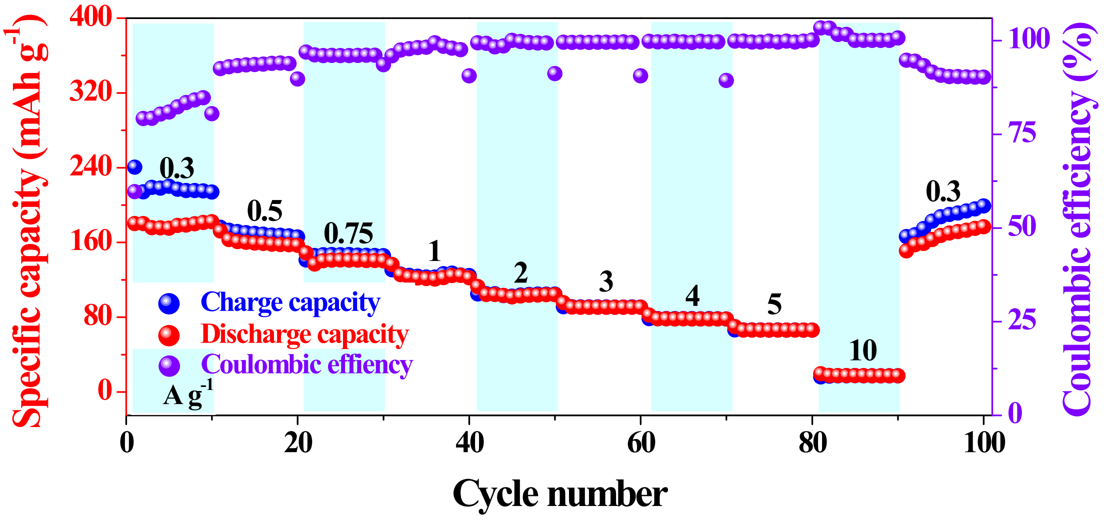

Fig. S17 Specific capabilities at various current densities for coin-type capacitors.

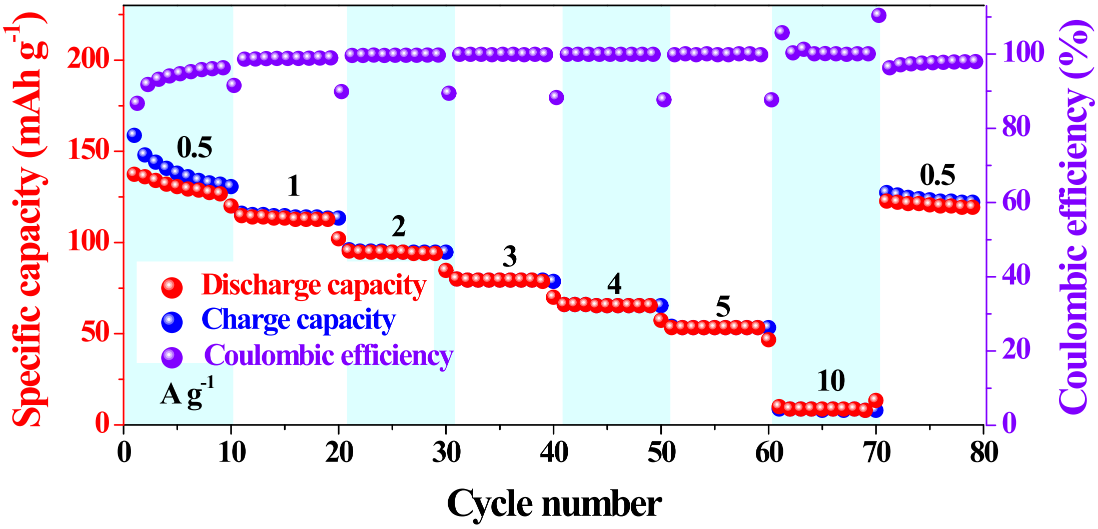

Fig. S18 Specific capabilities at various current densities for F-ZIHCs.

Table S1 The Brunauer-Emmett-Teller specific surface area (SBET) and pore volume (V_p) of the three samples.

Samples	BET-Surface area (m^2/g)	Pore volume (cm^3/g)	Average pore width (nm)
ARS	3.7688	2.565×10^{-2}	28
PGAF	29.4950	8.3453×10^{-2}	39
PGAF-ARS	13.4834	4.5195×10^{-2}	44

Table S2 The way of adsorption and adsorption energy.

PGAF-ARS	Parallel adsorption	Vertical adsorption
The adsorption energy (kcal/mol)	-38.26	-29.48

Table S3 The fitting calculation results.

	R_s (Ω)	R_{ct} (Ω)	Slope
PGAF-ARS	1.234	20.54	1.389
PGAF	1.276	29.57	1.087

Table S4 Comparison of the rate capability of PGAF-ARS electrode with other reported cathodes in Zn ion ESDs.[3-12]

Electrode	Capacity (mAh g^{-1}) @ (A g^{-1})	Cycle number @ Retention	Rate performance (mAh g^{-1}) @ (A g^{-1})	Ref.
PTCDI/rGO	120 @ 0.05 105 @ 5	150 @ 75%	117 @ 0.05 126 @ 0.1 131 @ 0.2 132 @ 0.5 131 @ 1 116 @ 2 137 @ 5	3
PC//AMX-AC	75.2 @ 0.44 26.4 @ 4.4	6000 @ 88.5%	75.2 @ 0.22 61.4 @ 0.44 53.8 @ 0.88 42.4 @ 2.2 33.7 @ 4.4	4
PDI-EDA/CB	118.0 @ 0.05	1500 @ 70.5%	118 @ 0.05 109 @ 0.1	5

			107 @ 0.2 104 @ 0.5 103 @1 100 @ 2 95 @ 5 107 @ 0.05	
ZVO	213 @ 0.05 76 @ 3	300 @ 68%	213 @ 0.05 164 @ 0.1 143 @ 0.3 120 @ 0.5 103 @ 0.8 80 @ 1 72 @ 2 51 @ 3 111 @ 0.5	6
DAA-GHF	172.3 @ 0.2 71.4 @ 50	5000 @ 92.5%	172 @ 0.2 134 @ 0.5 123 @ 1 121 @ 2 115 @ 5 107 @ 8 100 @ 10 97 @ 15 90 @ 20 81 @ 30 70 @ 40 147 @ 0.2	7
$ZnMn_2O_4$/NG	221 @ 0.1	2500 @ 97.4%	221 @ 0.1 205 @ 0.2	8

			166 @ 0.5 110 @1 75 @ 2 225 @ 0.1	
Zn/NixMn$_{3-x}$O$_4$ @ C	139.7 @ 0.05 98.5 @ 1.2	800 @ 93.5%	135 @ 0.05 131 @ 0.1 125 @ 0.2 122 @ 2 123 @ 0.2	9
1T-MoS$_2$/rGO	108.3 @ 5	1000 @ 88%	191 @ 0.1 168 @ 0.2 154 @ 0.5 137 @ 1 124 @ 2 108.3 @ 5 83 @ 10 186 @ 0.1	10
graphene @ PANI hydrogel	157 @ 0.1	6000 @ 80.5%	157 @ 0.1 155 @ 0.2 148 @ 0.5 141 @ 1 136 @ 2 127 @ 3 117 @ 4 106 @ 5 156 @ 0.1	11
PQ-FGH	161.2 @ 0.2	5000 @ 97.2%	161 @ 0.2 153 @ 0.4 148 @ 1	12

			145 @ 2 141 @ 5 138 @ 8 135 @ 10 129 @ 20 125 @ 30 120 @ 40 116 @ 50	
PGAF-ARS//Zn	230.4 @ 0.3 50.1 @ 30	10000 @ 92.6%	231.4 @ 0.3 211 @ 0.5 177 @ 0.75 167 @ 1 141 @ 2 120 @ 5 94 @ 10 68 @ 20 46 @ 30 200 @ 0.3	This work

References

1. F. Ma, Z. Hu, L. Jiao, X. Wang, Y. He, Y. Yang and Z. Li, *ACS Applied Energy Materials*, 2021, **4**, 5493-5503.
2. Y. Xie, X. Wang, L. Hou, X. Wang, Y. Zhang, C. Zhu, Z. Hu and M. He, *Journal of Energy Storage*, 2021, **38**, 102530.
3. N. Liu, X. Wu, Y. Zhang, Y. Yin, C. Sun, Y. Mao, L. Fan and N. Zhang, *Advanced Science)*, 2020, **7**, 2000146.
4. Z. Li, D. Guo, D. Wang, M. Sun and H. Sun, *Journal of Power Sources*, 2021, **506**, 230197.
5. B. Jiang, T. Huang, P. Yang, X. Xi, Y. Su, R. Liu and D. Wu, *Journal Colloid*

and Interface Science, 2021, **598**, 36-44.

6. C. Xia, J. Guo, Y. Lei, H. Liang, C. Zhao and H. N. Alshareef, *Advanced Materials*, 2018, **30**, 1705580.
7. H. Jiang, Y. Zhu, X. Ye, Z. Yue, L. Wang, J. Xia, J. Xie and C. Jia, *ACS Sustainable Chemistry & Engineering*, 2020, **8**, 9896-9905.
8. L. Chen, Z. Yang, H. Qin, X. Zeng and J. Meng, *Journal of Power Sources*, 2019, **425**, 162-169.
9. J. Long, J. Gu, Z. Yang, J. Mao, J. Hao, Z. Chen and Z. Guo, *Journal of Materials Chemistry A*, 2019, **7**, 17854-17866.
10. M. Huang, Y. Mai, G. Fan, X. Liang, Z. Fang and X. Jie, *Journal of Alloys and Compounds*, 2021, **871**, 159541.
11. J. Han, K. Wang, W. Liu, C. Li, X. Sun, X. Zhang, Y. An, S. Yi and Y. Ma, *Nanoscale*, 2018, **10**, 13083-13091.
12. H. Jiang, D. Yuan, D. Huang, B. Lin, J. Li, P. Guo and Y. Wang, *Applied Surface Science*, 2022, **585**, 152695.